ACS Sustainable Chemistry & Engineering

pubs.acs.org/journal/ascecg

Research Article

Nitrogen-Doped 3D Porous Composite GA/HNBRL Used as a Self-Supporting Electrode to Enhance the Adsorption and Conversion of Polysulfide in High-Capacity Li−S Batteries

Jixin Lu, Mengyuan Zhu, Cunguo Wang,* Lukuan Wang, Chunjie Wu, Yangyang Cui, Qiaoling Bi, Shaoyu Jiang, Qing Zhao, Xue Li, Aihua He,* Seung Hee Lee,* and Qi Li*

Cite This: https://doi.org/10.1021/acssuschemeng.5c06841

Read Online

ACCESS | Metrics & More | Article Recommendations | Supporting Information

ABSTRACT: The commercialization of lithium−sulfur batteries is limited by their low sulfur utilization rate and poor cycling stability. In this study, we successfully synthesized a nitrogen-doped porous aerogel material (GA/HNBRL) with high structural stability using graphene oxide (GO) as the carbon source and hydrogenated nitrile butadiene rubber latex (HNBRL) as a modifier. The synergistic effect of physical adsorption and chemical anchoring of GA/HNBRL carrier materials ensures high polysulfide adsorption and accelerated redox kinetics. Additionally, the incorporation of HNBRL enhances the mechanical properties of the carrier material, allowing for a higher sulfur loading and reducing the volume expansion of the active substance when used as a self-supporting material. The S@GA/HNBRL electrode material was prepared and could achieve an initial discharge specific capacity of 1315.6 mAh/g at a rate of 0.1 C without the involvement of current collectors, conductive agents, and binders. After 300 cycles at 0.1 C, its discharge specific capacity can still reach 870.9 mAh/g. In particular, the battery can still achieve a discharge specific capacity of 423.3 mAh/g after 500 cycles at a 1 C rate. This study provides a new approach for the application research of self-supporting materials in lithium−sulfur batteries by combining controllable porous structures with higher conductivity polymer materials.

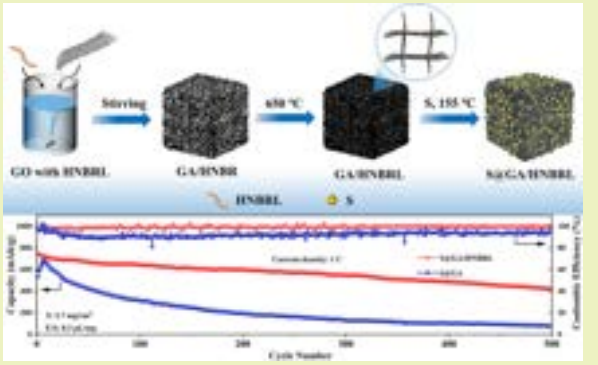

KEYWORDS: *Graphene aerogel, Hydrogenated nitrile butadiene rubber latex, Self-supporting material, Polysulfide, Lithium−sulfur battery*

INTRODUCTION

With the development of society and the rapid growth of the global economy, exploitable reserves of fossil fuels are gradually diminishing. Lithium-ion batteries have advantages such as a high operating voltage, good cycling stability, and long service life, and they are widely used in various fields.[1−7] However, the theoretical capacity of these materials is relatively low, and they are no longer able to meet the increasing demands of emerging industries such as smart grids for electrochemical energy storage solutions.[8−11] Therefore, the development of new secondary batteries with high energy density and low self-discharge rates, such as lithium−sulfur, sodium-ion, magnesium-ion, and zinc-ion batteries, is of great significance.[12−18] Among the numerous secondary batteries, lithium−sulfur batteries (LSBs) have higher energy density (2600 Wh/kg) and theoretical specific capacity (1675 mAh/g).[19−21] Sulfur is abundant in the Earth's crust and has been extracted for thousands of years. These advantages make LSBs highly valuable for research and hold significant commercial potential for next-generation energy storage applications.[22−24] However, because of the physical and chemical characteristics of S and the complicated electrochemical reactions during charge and discharge, the practical commercialization of LSBs faces numerous challenges, including the poor electrical conductivity of sulfur, the "shuttle effect", and volume expansion induced by the soluble lithium polysulfides (LiPSs) generated during the reaction.[25−27]

To overcome these drawbacks, researchers have developed materials with different structures for use in positive electrodes, separators, and electrolytes.[28,29] Currently, in the research of positive electrode materials, efforts have been made to encapsulate active materials in different matrices, including carbon based materials, conductive polymers, and metal

Received: July 7, 2025
Revised: November 17, 2025
Accepted: November 17, 2025

oxides.[30−32] In carbon materials, graphene has received widespread attention as a support or substrate for LSB cathodes because of its outstanding conductivity, mechanical flexibility, and large specific surface area. Recent studies have shown that graphene−sulfur hybrid materials greatly improve the electrochemical performance. The conventional approach of LSB cathodes is to evenly combine the electrode material, conductive additive, and binder, dissolve them in an organic solvent such as *N*-methylpyrrolidone (NMP), and then coat them on a current collector. The introduction of a conductive additive and binder adds mass to the cathode, thereby reducing the energy density of the cathode. The presence of a binder may clog the carrier material pores and raise its resistance. Moreover, if the content of the binder is inappropriate, the surface slurry can peel off because of uneven mechanical strength.[33] Flexible self-supporting electrodes efficiently utilize the electrode area without collectors. Importantly, the flexible self-supporting sulfur electrode eliminate the toxic effects associated with NMP used in traditional coating methods.[34−36] Some researchers have synthesized self-supporting materials with three-dimensional porous structures using graphene as the matrix material.[37−39] The distinctive feature of this electrode is that its preparation process does not require adhesives or conductive agents, and it can accommodate a large amount of sulfur while ensuring excellent conductivity.[40,41] However, due to the difference in density between S and Li_2S, the volume of the active material will undergo significant changes during the charging and discharging process of the battery.[42] If the mechanical stability of the carrier material is poor, the repeated volumetric change process of the active material may cause the entire positive electrode structure to collapse, thereby reducing the cycling performance of the cells. This is crucial for self-supporting carrier materials.

Given this, for the first time, we used hydrogenated nitrile butadiene rubber latex (HNBRL) as a modifier and graphene oxide (GO) as a carbon source to successfully synthesize a novel composite material (GA/HNBRL) with a three-dimensional porous structure through self-assembly and applied it to LSBs. The rich pore structure of GA/HNBRL offers ample space for S volume change and achieves high sulfur loading. The 3D conductive framework established by interweaving graphene facilitates electrolyte infiltration and rapid ion and electron transport. The presence of oxygen-containing groups and N atoms can effectively adsorb polysulfides, thereby suppressing the shuttle effect. Moreover, with the participation of nitrile latex, the mechanical strength of the aerogel was significantly improved, and the structural stability of cathode materials was improved. Based on test results, the specific capacity of lithium−sulfur batteries based on S@GA/HNBRL electrodes reaches 1315.6 mAh/g at 0.1 C. After 300 cycles, the reversible capacity of the battery remained at 870.9 mAh/g, and the average capacity degradation rate per cycle was about 0.11%.

EXPERIMENTAL SECTION

Preparation of GA/HNBRL and GA. The experiment used 800 mesh natural graphite as a raw material to prepare graphene oxide using an improved Hummers method. First, 4 mL of 6 mg/mL graphene oxide solution was taken into a small beaker, and HNBR latex and ascorbic acid were added in a mass ratio of 1:1.5:1. Once uniformly mixed, 1 mL of 60 mg/mL sodium dodecyl sulfate (SDS) solution was added, and then magnetic stirring was performed. When fine bubbles were generated in the beaker, the beaker was immediately moved to a 70 °C oven to further reduce the graphene oxide. After 2 h of reaction, the beaker was moved to a −20 °C freezer for 7 h, and then the material was into a 90 °C oven for 4 h of reaction. It was allowed to cool before it was removed and then washed with ethanol. After several washings with deionized water, the GA/HNBRL composite material was put into a quartz tube heated at 650 °C for 2 h under a nitrogen atmosphere. Once completely cooled, the ultralight and highly conductive composite material was obtained. The preparation process of the graphene aerogel (GA) material was the same as that of GA/HNBRL, except that hydrogenated nitrile butadiene rubber latex was not added.

Preparation of S@GA/HNBRL and S@GA. First, a slicing machine was used to cut the aforementioned samples into thin slices measuring 3 mm thick and 13 mm in diameter. The mass of each sample slice was weighed and recorded. Then, sulfur powder was weighed in a 7:3 mass ratio (S:GA/HNBRL) and placed into a small beaker. A sufficient amount of CS_2 solution was added to completely dissolve the sulfur. Subsequently, the sliced GA/HNBRL aerogel sheets were placed into the beaker for 2 h to ensure maximum sulfur adsorption. Then, the samples were transferred to a vacuum drying oven at 60 °C, and the temperature was maintained for 6 h to evaporate residual CS_2 solution. Finally, the sample was transferred to a closed reactor and heated at 155 °C for 12 h. Once completely cooled, the S@GA/HNBRL composite cathode material was obtained (Figure S1). The preparation process of S@GA was basically the same as that of S@GA/HNBRL, except that the GA/HNBRL material was replaced with GA. The sulfur loading on each electrode was 2−2.7 mg/cm^2.

Preparation of Li_2S_6 Solution. Sulfur and Li_2S were mixed in a 1:5 molar ratio and then dissolved in a solution of 1,3-dioxolane/1,2-dimethoxyethane (DOL/DME, 1:1 in vol, 2.0 wt % $LiNO_3$ + 1.0 M LiTFSI). It was stirred at 60 °C for 12 h to obtain the Li_2S_6 solution.

Adsorption Test. Li_2S and S were dissolved in DME and DOL (v/v = 1:1, 2.0 wt % $LiNO_3$ + 1.0 M LiTFSI) in a molar ratio of 1:5 to prepare a Li_2S_6 solution with a concentration of 0.2 M. GA and GA/HNBRL of the same mass were added to 5 mL of the prepared Li_2S_6 solution, which was left standing for 6 h. The color change was recorded with a camera.

RESULTS AND DISCUSSION

Structural Characterization. The electrochemical performance of the enhancement mechanism for the prepared positive electrode material is shown in Figure 1. Although GA has high conductivity and a rich pore structure, its inherent electronegativity is weak, making it unable to effectively adsorb polysulfides, resulting in a low sulfur utilization rate (Figure 1A). In contrast, the doping of N atoms into GA/HNBRL exhibits high electronegativity and can generate strong interactions with polysulfides, increasing the contact area

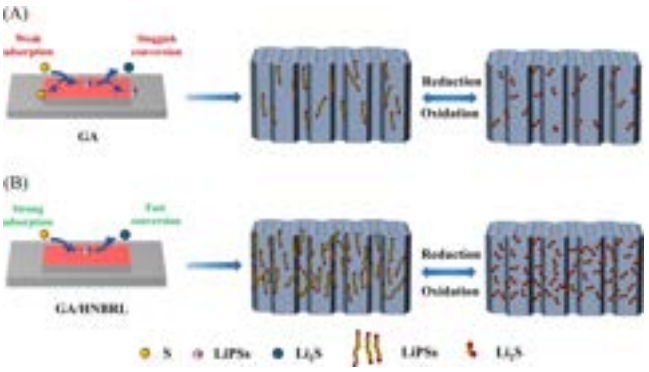

Figure 1. Working mechanisms for polysulfide adsorption and conversion of (A) GA and (B) GA/HNBRL.

https://doi.org/10.1021/acssuschemeng.5c06841
ACS Sustainable Chem. Eng. XXXX, XXX, XXX−XXX

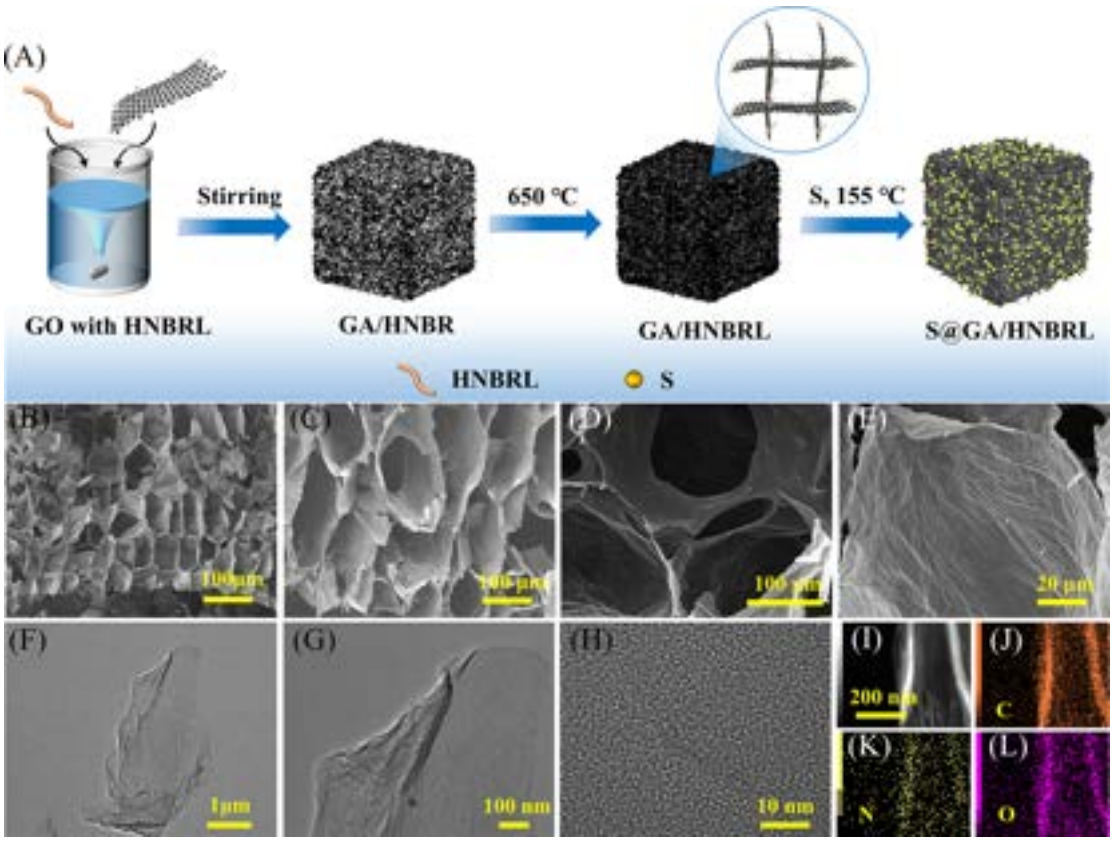

Figure 2. (A) Schematic illustration of the procedure for the synthesis of S@GA/HNBRL. (B) SEM image of GA. (C−E) SEM images of GA/HNBRL. (F, G) TEM images of GA/HNBRL at different magnifications. (H) HR-TEM image of GA/HNBRL. (I) HAADF-STEM image of GA/HNBRL. EDS color mapping of GA/HNBRL: (J) carbon, (K) nitrogen, and (L) oxygen.

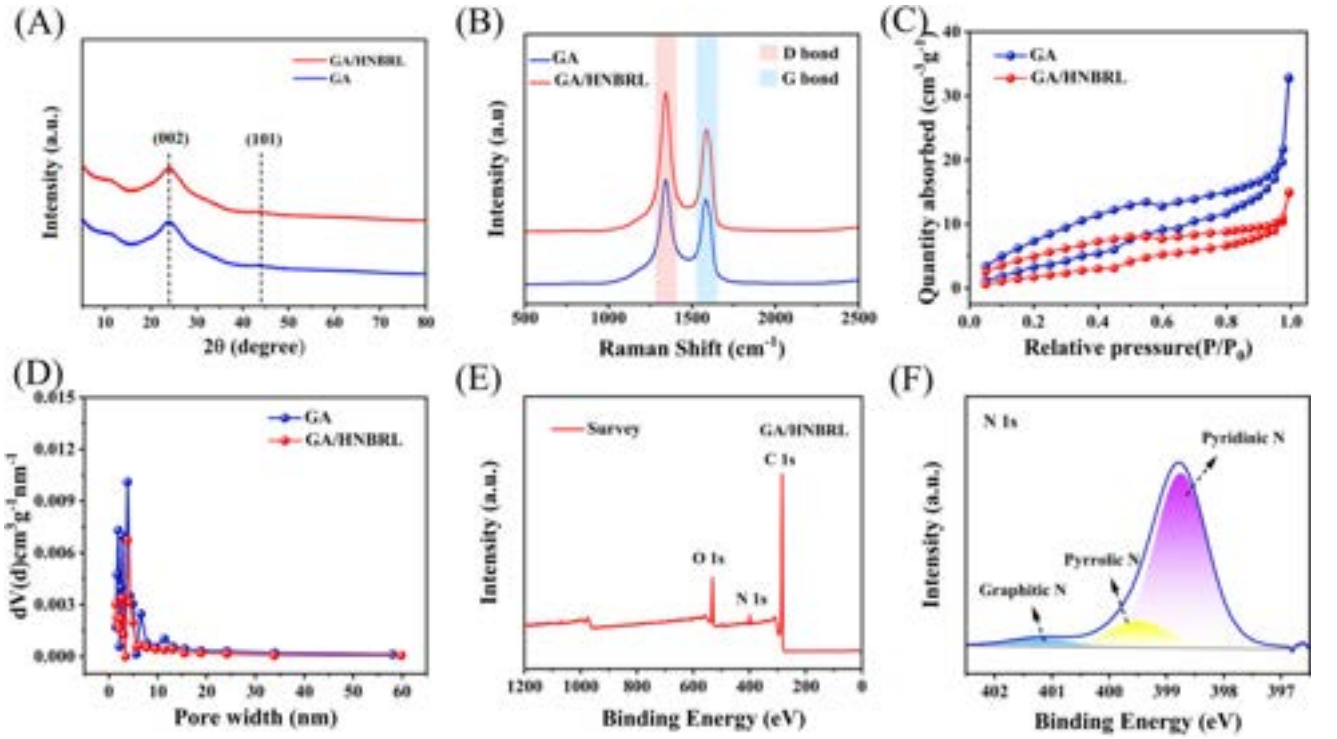

Figure 3. (A) XRD patterns of GA/HNBRL and GA. (B) Raman profiles of GA and GA/HNBRL. (C) Nitrogen adsorption−desorption curves of GA/HNBRL and GA. (D) Pore size distribution of GA/HNBRL and GA. (E) Survey XPS spectrum of GA/HNBRL. (F) High-resolution XPS spectrum of N 1s for GA/HNBRL.

https://doi.org/10.1021/acssuschemeng.5c06841
ACS Sustainable Chem. Eng. XXXX, XXX, XXX−XXX

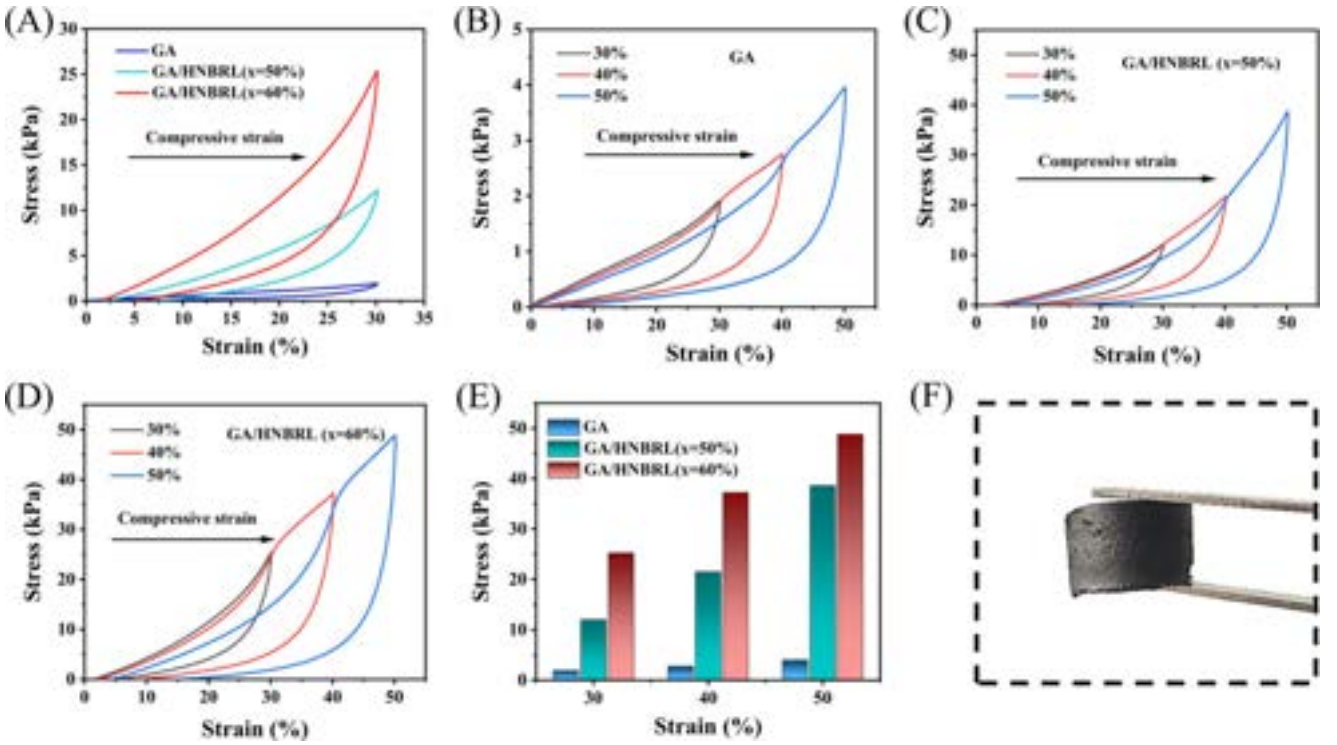

Figure 4. (A) Comparison of mechanical properties of materials with different latex contents under 30% compression deformation. Stress−strain curves of (B) GA, (C) GA/HNBRL (x = 50%), and (D) GA/HNBRL (x = 60%) under compression. (E) Comparison of mechanical properties of materials with different latex contents under different compression deformations. (F) Optical image of GA/HNBRL.

between intermediate products and carrier materials, thereby achieving the rapid conversion of polysulfides (Figure 1B).

Figure 2A shows the synthesis process of a three-dimensional S@GA/HNBRL composite material. Graphene oxide and hydrogenated nitrile rubber were used as carbon and nitrogen sources, respectively. Using sodium dodecyl sulfate (SDS) as a foaming agent, a three-dimensional microstructure of the carbon skeleton was formed with the assistance of a freeze-drying process. Afterward, GA/HNBRL was placed into a tube furnace and subjected to carbonization under an argon atmosphere to further enhance the conductivity of the material. Finally, the obtained GA/HNBRL material was compounded with sulfur at 155 °C to obtain the self-supporting S@GA/HNBRL electrode.

The structure and morphology of GA and GA/HNBRL were characterized by using field emission scanning electron microscopy (FE-SEM). Figure 2B,C shows the SEM images of GA and GA/HNBRL at low magnification, respectively. It can be seen that both materials form honeycomb-like porous structures; however, the pure graphene aerogel has poor toughness, and the porous structures are easily broken. Compared with GA, GA/HNBRL has enhanced material toughness and more uniform and regular structures due to the involvement of nitrile latex, which indicates that its mechanical stability is higher. Figure 2D,E shows the SEM images of GA/HNBRL at higher magnification. It can be observed that the graphene layers are interlaced, forming a rich network structure, and there are many folds on the thin wall. This special fold structure not only provides an attachment point for sulfur but also increases the contact area between the sulfide and the electrolyte, thereby achieving rapid electron ion transfer. As shown in Figure 2F,G, the TEM images of GA/HNBRL at different magnifications reveal that the carbonized GA/HNBRL exhibits a characteristic wrinkled, ultrathin layered morphology consistent with typical graphene-like materials. High-resolution TEM imaging (Figure 2H) further discloses the presence of disordered carbon lattice structures within the material. Such disordered regions are typically closely associated with heteroatom doping and defect engineering. The HAADF-STEM image (Figure 2I) and its corresponding EDS elemental distribution maps (Figure 2J−L) demonstrate the homogeneous distribution of oxygen, nitrogen, and carbon across the flakes. The homogeneously distributed nitrogen signal indicates the effective introduction of nitrogen into the GO framework. This uniform elemental distribution ensures the presence of abundant catalytically active sites within the material, thereby promoting the adsorption and transformation of polysulfides.

The crystallinity of GA and GA/HNBRL was analyzed by using X-ray diffraction (XRD) patterns (Figure 3A). It can be seen that two diffraction peaks appear near 25° and 44° for both materials, which correspond to the characteristic peaks of the (002) and (101) crystal planes of graphite materials.[43−45] This demonstrates that the materials have a certain degree of graphitization after high-temperature heat treatment and good conductivity, which is crucial for electron and ion transport. The Raman spectra of GA and GA/HNBRL materials are shown in Figure 3B, revealing two distinct characteristic peaks at 1345 and 1587 cm^{-1} in the Raman spectra, attributed to the D band and G band of graphitic carbon, respectively.[46] The intensity ratio of the GA/HNBRL band to the G band (I_D/I_G) is approximately 1.34, which is higher than that of the GA material (1.22). This indicates that abundant defect structures have been generated in the carbon network during the nitrogen atom doping process.[47]

https://doi.org/10.1021/acssuschemeng.5c06841
ACS Sustainable Chem. Eng. XXXX, XXX, XXX−XXX

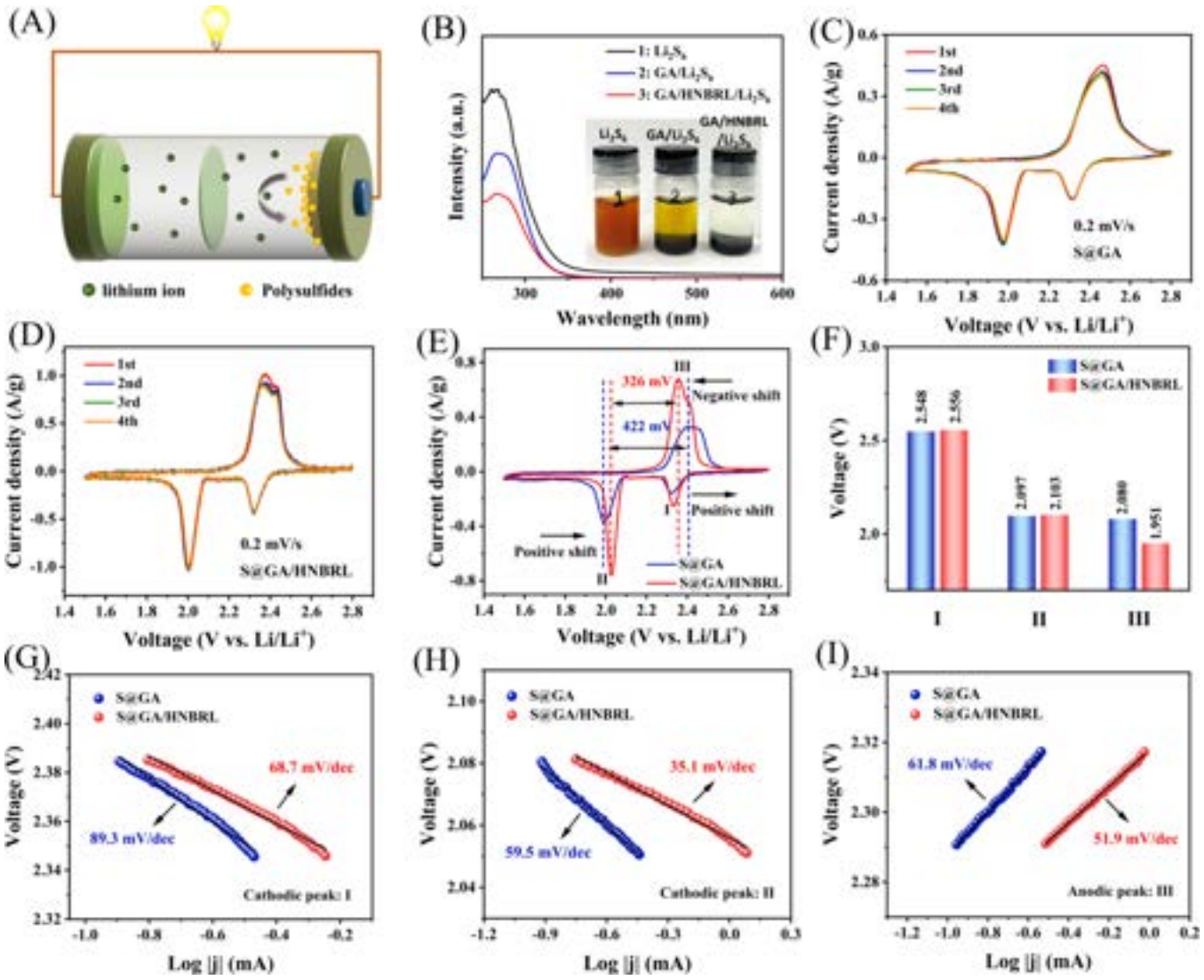

Figure 5. (A) Schematic illustration of the synergistic adsorption−catalytic effect of GA/HNBRL on polysulfides. (B) UV−vis spectra of Li_2S_6 in DOL and DME solutions and after interacting with the GA and GA/HNBRL, respectively. The inset image shows the corresponding Li_2S_6 solution with absorbers. CV cycling stability testing of (C) S@GA and (D) S@GA/HNBRL electrodes at 0.2 mV/s. (E) CV curves of S@GA and S@GA/HNBRL electrodes at 0.1 mV/s. (F) Onset potential of GA and GA/HNBRL based coin cells. Tafel plots of (G) peak I, (H) peak II, and (I) peak III.

Figure 3C shows the nitrogen adsorption−desorption curves of GA/HNBRL and GA. The specific surface area of GA is 28.49 m^2/g, and the pore volume is 0.057 cm^3/g. The specific surface area of GA/HNBRL is 16.90 m^2/g, and the pore volume is 0.027 cm^3/g. Figure 3D shows the pore size distribution curves of GA/HNBRL and GA. It can be seen that the pore sizes of GA/HNBRL and GA are primarily centered around 3.8 nm. It is demonstrated that both GA and GA/HNBRL materials possess a certain degree of mesoporous structure internally.[48] Furthermore, FE-SEM images of GA/HNBRL and GA reveal that within both materials, a rich macroporous structure is formed by the interweaving of two-dimensional graphene oxide sheets (Figure 2B−E). The rich porous structure not only facilitates rapid electrolyte infiltration but also allows the carrier material to adsorb more active substances, increasing the loading amount of active sulfur. To verify complete SDS removal, we supplemented the analysis with infrared testing (Figure S2). As observed, the characteristic SDS peaks (1469, 1276, and 1080 cm^{-1}) completely disappeared in the GA/HNBRL spectrum, with only GA/HNBRL framework-related peaks (e.g., 1628 cm^{-1}, 1728 cm^{-1}) retained. Additionally, no characteristic peaks for sodium and sulfur were observed in the XPS survey spectrum of GA/HNBRL (Figure 3E). This indicates that SDS was fully decomposed and removed during carbonization.

In order to determine the sulfur content in S@GA/HNBRL composite materials, the thermogravimetric analysis testing method was used for testing and analysis (Figure S3). When the testing temperature was increased to around 280 °C, the weight loss rate of S@GA/HNBRL reached 70%. This indicates that the mass proportion of sulfur in the composite material is 70%, which is consistent with the experimental mass ratio of 3:7 (GA/HNBRL:S).

The elemental composition and surface chemical state of GA and GA/HNBRL were studied by performing X-ray photoelectron spectroscopy (XPS) measurements. Compared with GA, three elements (carbon, nitrogen, and oxygen) appeared in the test spectrum of GA/HNBRL, indicating that GO is

https://doi.org/10.1021/acssuschemeng.5c06841
ACS Sustainable Chem. Eng. XXXX, XXX, XXX−XXX

successfully combined with HNBRL (Figure 3E and Figure S4). The spectrum of C 1s can be deconvolved into three different peaks, with binding energies of 284.8, 285.8, and 287.9 eV, corresponding to C−C, C−N, and O—C═O bonds, respectively[46] (Figure S5). The spectrum of N 1s can be deconvolved into three different peaks, with binding energies of 398.8, 399.5, and 401.5 eV, corresponding to pyridinic N, pyrrolic N, and graphitic N, respectively[12,49] (Figure 3F). The nitrogen doping amount on the carbon substrate reached 3.11%, indicating the formation of a carbon and nitrogen framework material, thereby improving the adsorption performance of the host material for polysulfides.[50,51]

To assess the impact of HNBRL on the mechanical properties of the material, we also conducted compression deformation tests on the material. As shown in Figure 4A, pure GA material exhibits lower resilience at 30% compressive strain, and the compressive stress also improves with the increase in latex content. When the compression deformation of the material reaches 50%, the compression stress of GA is about 4 kPa. In contrast, the compression stress of GA/HNBRL (x = 60%) can reach 50 kPa (x = 60% means that the mass ratio of GO to HNBRL is 1:1.5), which is more than 10 times that of the GA material (Figure 4B−E). As shown in Video S1, GA/HNBRL still has an excellent rebound ability under large compression deformation, and the height of the material before and after compression remains in an almost unchanged state (Figure S6A,B), indicating that the introduction of HNBRL can greatly improve the structural stability of aerogels, thereby inhibiting the volume expansion of active materials and reducing the damage to the host material structure caused by volume changes. Figure 4F is an optical image of GA/HNBRL. It can be seen that the macroscopic structure of the material is also complete, and there are no damaged defects on the surface of the GA/HNBRL material.

Electrochemical Performance. Figure 5A presents the mechanism behind the enhanced electrochemical performance of the assembled LSBs. The doping of N atoms can enhance the adsorption capacity of GA/HNBRL for LiPSs and limit their diffusion toward the anode side. Moreover, the porous structure composed of GO and HNBRL can provide an efficient channel for the transport of Li ions.

The adsorption capacity for Li_2S_6 is essential for determining the effectiveness of carrier materials in inhibiting the shuttle effect. Observation experiments were performed to compare the adsorption capacities of GA/HNBRL and GA toward polysulfides. Equal weights of GA/HNBRL and GA materials were placed in sealed vials containing 0.2 M Li_2S_6 solution. After 6 h of incubation, the solution in the vial containing GA/HNBRL exhibited a more pronounced color change, becoming transparent. Following adsorption, the supernatant from each vial was collected for UV measurement. The Figure 5B shows the characteristic peak of Li_2S_6 at approximately 270 nm, where the blank Li_2S_6 showed the highest absorption intensity. Meanwhile, the solution adsorbed by GA/HNBRL displayed a low absorption intensity, revealing its high adsorption capacity for LiPSs. To further investigate the reaction mechanisms in polysulfide adsorption and conversion, the lower layer samples were collected after adsorption experiments and dried at 80 °C for 24 h, followed by XPS analysis. The XPS measurement spectrum of GA/HNBRL/Li_2S_6 revealed the existence of carbon, oxygen, nitrogen, fluorine, sulfur, and lithium elements in the sample (Figure S7A). Furthermore, compared with the state prior to Li_2S_6 adsorption, the N 1s orbital spectrum of GA/HNBRL/Li_2S_6 exhibits a pronounced shift toward higher binding energies (Figure S7B). This is attributed to chemical coordination or strong polar interactions between nitrogen (particularly pyridinic N and some pyrrolic N) and Li_2S_6, which weaken the S−S bonds in the adsorbed polysulfide to reduce its conversion activation energy. This leads to a decrease in electron density around nitrogen coupled with local charge redistribution. Consequently, all nitrogen peaks collectively shifted toward higher binding energies. These results indicate that nitrogen in GA/HNBRL participates in the anchoring and conversion processes of LiPSs.

The reversibility of electrochemical reactions in batteries can be tested by using cyclic voltammetry (CV). Figure 5C,D shows the cyclic voltammetry curves of the S@GA and S@GA/HNBRL electrodes at 0.2 mV/s. It can be seen that the CV curve of the S@GA/HNBRL has higher overlap from the first to the fourth cycle, with no significant shift in peak potential, indicating that the S@GA/HNBRL electrode has excellent reversibility. Furthermore, it can also be observed from the graph that as the test progresses, the closed area of the CV curve in the fourth cycle decays to a certain extent compared with the first cycle. As the closed area represents the capacity of the cell, the attenuation of the closed area also indicates that the battery's capacity has decayed to a certain extent after continuous testing.

Figure 5E shows the CV test curves of the two electrode materials, where the two cathodic peaks of the S@GA electrode appear at the positions 2.32 and 1.98 V, respectively, corresponding to the transformation process from sulfur to soluble lithium polysulfide and from long-chain lithium polysulfide to Li_2S.[12,23,52] During the forward scanning process, S@GA exhibited a strong anodic peak at 2.41 V, representing the conversion reaction of Li_2S into S_8. The two reduction peaks of the S@GA/HNBRL electrode appeared at 2.33 and 2.03 V, respectively. Compared with the S@GA electrode, the second cathodic peak shifted to the right by about 50 mV. The anodic peak of the S@GA/HNBRL electrode appears at 2.35 V, and compared to the 2.41 V of the S@GA electrode, the potential shifts to the left by about 60 mV. Both the positive shift of the cathodic peak and the negative shift of the anodic peak indicate that the lithium−sulfur battery assembled based on the S@GA/HNBRL electrode has better reversibility and a faster electrochemical transformation rate, which improves the charging and electrochemical performance of the cell. Compared with the S@GA/HNBRL electrode, the S@GA electrode exhibits a lower current in both cathodic and anodic peaks (Figure S8), which reflects that the S@GA electrode has poor redox reaction activity. Moreover, the catalytic performance of the S@GA and S@GA/HNBRL electrodes was evaluated by the onset potential at a current density of 10 $\mu A/cm^2$ above the baseline (Figures S9 and S10). Figure 5F illustrates that the S@GA/HNBRL electrode displays higher onset potentials in reduction and lower onset potentials in oxidation peaks, reflecting a reduced overpotential for LiPS redox conversion.

Figure S11A−C shows the locally enlarged CV curves of the S@GA and S@GA/HNBRL electrodes, respectively. It can be seen that the S@GA/HNBRL electrode has a significant current variation at the initial stage of each reaction, indicating that its reaction is higher. The Tafel curves were obtained (Figure 5G−I) to further evaluate the electrocatalytic behavior of the carrier material in the LiPS oxidation−reduction

https://doi.org/10.1021/acssuschemeng.5c06841
ACS Sustainable Chem. Eng. XXXX, XXX, XXX−XXX

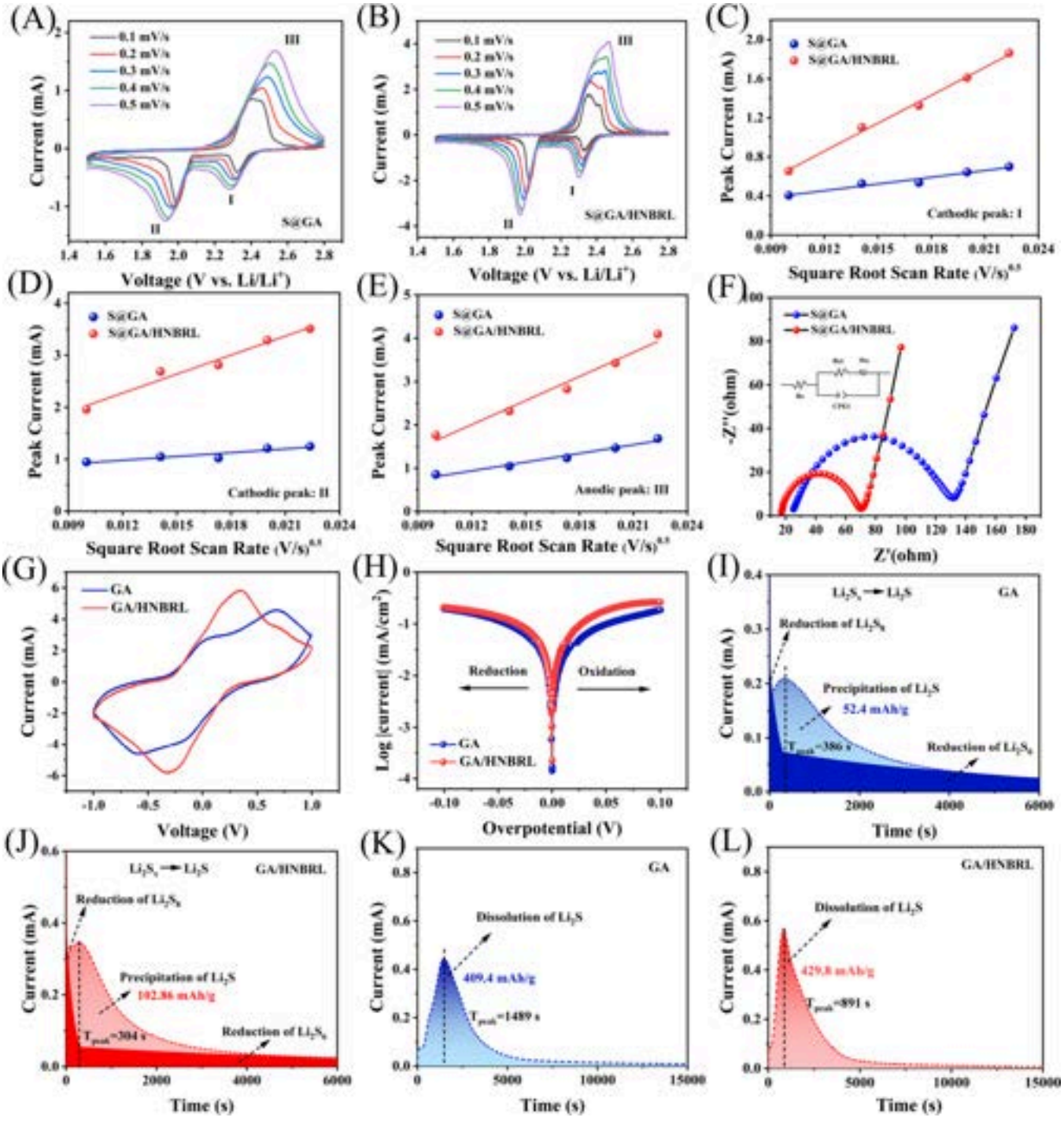

Figure 6. (A) The CV curves of the S@GA electrode and (B) S@GA/HNBRL electrode at 0.1−0.5 mV/s. (C−E) CV peak current values of peaks I, II, and III for S@GA and S@GA/HNBRL electrodes versus square root of the scan rate. (F) EIS curves of S@GA and S@GA/HNBRL. (G) CV curves of symmetric cells based on different sulfur hosts. (H) Tafel plots of symmetric cells. Li_2S nucleation curves on (I) GA and (J) GA/HNBRL at 2.06 V. Li_2S decomposition curves on (K) GA and (L) GA/HNBRL at 2.4 V.

process.[53] The fitting slopes of the cathodic peaks (I and II) and anodic peak (III) of the GA/HNBRL electrode are 68.7, 35.1, and 51.9 mV/dec, respectively, values that are lower than those of the GA electrode (89.3, 59.5, and 61.8 mV/dec, correspondingly), indicating that the mutual enhancement of the porous structure and physical and chemical adsorption of N atoms enables the rapid conversion of lithium polysulfides.[54]

To examine the lithium-ion diffusion behavior of lithium ions in different electrodes, we performed CV at different scan rates ranging from 0.1 to 0.5 mV/s (Figure 6A,B). The preservation of the CV shape further confirms the electrochemical stability of GA/HNBRL. In addition, the peak current was plotted against the square root of the scan rate, which showed a clear linear relationship. From the figures, it can be seen that as the scanning rate increases, the anodic peak moves toward the positive potential direction and the cathodic peaks move toward the negative potential direction. During this process, the polarization voltage increases. The diffusion

https://doi.org/10.1021/acssuschemeng.5c06841
ACS Sustainable Chem. Eng. XXXX, XXX, XXX−XXX

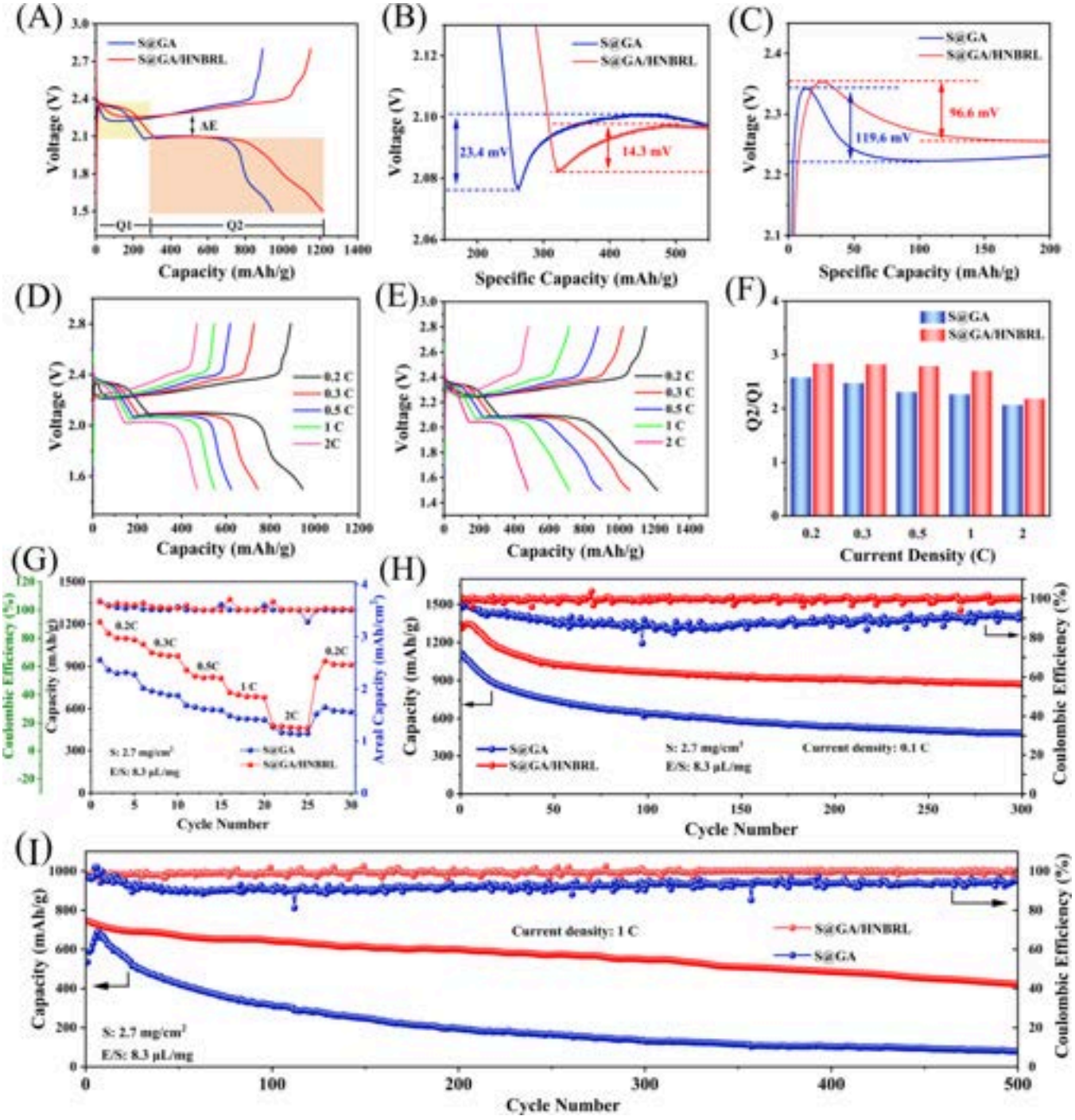

Figure 7. (A) Charge−discharge curves of S@GA and S@GA/HNBRL electrodes at a rate of 0.2 C. (B) Discharge and (C) charge profiles at the initial stage. (D) Charge−discharge curves of S@GA electrode at different rates. (E) Charge−discharge curves of S@GA/HNBRL electrode at different rates. (F) The values of Q2/Q1 at different rates. (G) The comparison of rate performance between S@GA and S@GA/HNBRL electrodes. (H) Cycling performance of S@GA and S@GA/HNBRL electrodes at 0.1 C. (I) Long-term cycling performance of Li−S batteries with different electrodes at 1 C.

efficiency of lithium ions is calculated using the Randles−Sevcik formula:[12,49,55]

$$I_p = (2.69 \times 10^5) n^{1.5} S D_{Li+}{}^{0.5} \Delta C_{Li+} \nu^{0.5} \quad (1)$$

where I_p and ν represent the peak current, respectively. Since the electron transfer number n, the geometrical area S of the sulfur electrode, and the lithium-ion concentration C_{Li+} are all constant values, I_p of all peaks increased linearly with increasing square root of the scan rate.[45] The slope of the S@GA/HNBRL electrode is higher than that of the S@GA, revealing a more efficient lithium-ion diffusion ability (Figure 6C−E). The improvement of the lithium-ion diffusion ability can be explained as follows: (1) The incorporation of nitrogen improves the adsorption capacity of the carrier material for polysulfides, improves interfacial wettability, and accelerates the transfer rate of ions. (2) Introducing nitrogen atoms can

https://doi.org/10.1021/acssuschemeng.5c06841
ACS Sustainable Chem. Eng. XXXX, XXX, XXX−XXX

improve the electrocatalytic behavior of materials toward LiPSs and reduce the reaction potential barrier.

To visually compare the electrical conductivity of different materials, we measured the conductivity of GA and GA/HNBRL using a four-point probe method with results presented in Table S1 (Supporting Information). Test results indicate that GA/HNBRL exhibits a resistivity of 8 Ω·cm and a conductivity of 0.125 S/cm, demonstrating superior electrical conductivity compared to those of GA of 10 Ω·cm and 0.1 S/cm, respectively. The transfer rate of electrons/ions can be evaluated through electrochemical impedance (EIS). Figure 6F shows the EIS curves and associated circuit simulations of the two electrode materials S@GA and S@GA/HNBRL, respectively. The EIS curves feature a semicircle at high frequencies and a straight line at low frequencies, associated with the charge transfer resistance (R_{ct}) and ion diffusion resistance (R_s) of the electrode material, respectively. The EIS data fitting results for the S@GA and S@GA/HNBRL electrodes are shown in Table S2. The R_{ct} of the S@GA electrode material is about 102.2 Ω, and the ion diffusion resistance is about 24.37 Ω. Compared with the S@GA electrode material, the S@GA/HNBRL electrode material has a smaller charge transfer resistance with a resistance value of 50.5 Ω. The ion diffusion resistance is 16.56 Ω, indicating that the introduction of multielectron N atoms reduces the R_{ct} of the material, which improves the ion and electron transfer rates and thus accelerates the redox reaction.

To verify the catalytic activity of GA/HNBRL on LiPSs, a symmetric battery was assembled using 0.2 M Li_2S_6 dissolved in DOL/DME electrolyte. The cyclic voltammetry (CV) curve of GA/HNBRL shows that compared with the GA single material, the current density of the GA/HNBRL composite material is higher, indicating a significant improvement in the reaction kinetics of polysulfides (Figure 6G). These results indicate that the GA/HNBRL composite structure has high catalytic activity in the liquid−solid conversion process.[56] Tafel plots were obtained to further validate the electrocatalytic behavior of GA/HNBRL toward LiPS conversion (Figure 6H). The value of the exchange current density (I_0) was calculated from the Butler−Volmer equation as shown below:[23,57]

$$\eta = a + b \times \log I \tag{2}$$

where a is a constant, b is the Tafel slope, η is the overpotential, and I is the response current of symmetric cells.[46] The GA/HNBRL showed the highest I_0 during redox processes of 0.15 mA/cm^2, which is higher than that of GA (0.085 mA/cm^2). Moreover, the reduced Tafel slope of the GA/HNBRL battery demonstrates its superior catalytic capability in facilitating conversion reactions.

In general, the transition process from Li_2S_4 to Li_2S accounts for three-quarters of the theoretical capacity of the battery. Therefore, rapid and uniform Li_2S nucleation is crucial for enhancing battery performance.[21,58] To test the effect of GA/HNBRL on the transformation of LiPSs, we performed nucleation experiments on Li_2S. The host material was used as the cathode, and Li foil and Li_2S_8 electrolyte were used as the anode and electrolyte, respectively. First, the cell was discharged at a constant current of 2.07 V to create adequate overpotential for Li_2S nucleation. Subsequently, the discharge was continued at 2.06 V with continuous current recording. The GA/HNBRL cathode revealed a higher deposition capacity of 102.86 mAh/g, which is superior to that of the GA cathode of 52.4 mAh/g (Figure 6I,J). Moreover, the cell with GA/HNBRL has a sharper peak within the shortest time (304 s). This result confirms that the nitrogen-doped porous materials promote faster LiPS conversion and contribute to a higher specific capacity in LSBs. Moreover, Li_2S decomposition experiments were performed to explore the kinetics (Figure 6K,L). The GA/HNBRL cathode exhibited a higher peak current than the GA cathode, reflecting its smaller overpotential for Li_2S dissolution.[23,59] In addition, GA/HNBRL exhibited a higher Li_2S decomposition capacity (429.8 mAh/g) compared to GA (409.4 mAh/g). It was revealed that the nitrogen-rich porous structure can enhance the oxidation reaction kinetics of Li_2S.

To further investigate the influence of different materials (GA and GA/HNBRL) on lithium sulfide decomposition, we employed the galvanostatic intermittent titration technique (GITT) for supplementary studies. The internal resistance (IR) of the cells was determined using the following equation:

$$\mathrm{IR} = \frac{V_{\mathrm{QOCV}} - V_{\mathrm{CCV}}}{I_{(\mathrm{applied})}} \tag{3}$$

where $I_{(\mathrm{applied})}$ is the applied discharge current, V_{CCV} is the closed-circuit voltage, and V_{QOCV} is the quasi-open-circuit voltage.[12] As shown in Figure S12, during the nucleation and decomposition of lithium sulfide, the S@GA/HNBRL based battery exhibits a lower IR compared to the S@GA based battery, indicating that GA/HNBRL exerts a stronger promoting effect on the conversion of sulfides.

To evaluate the specific capacity of LSBs, galvanostatic charge−discharge (GCD) curves of all cathodes were recorded at 0.2 C (Figure 7A). The first GCD curves of the S@GA and S@GA/HNBRL electrodes exhibit comparable charging and discharging platforms. At the position near 2.3 V, they both have shorter platforms, which represents the transformation process from S_8 to soluble lithium polysulfide. Then, a longer flatter platform appears at 2.1 V, representing the transformation process from lithium polysulfide to the final product Li_2S. When the discharge process is complete, the battery enters the charging stage. While the charging voltage increases to around 2.3 V, a long flat plateau appears on the charging curve, which corresponds to the conversion process from lithium sulfide to S. The discharge specific capacity of the S@GA/HNBRL battery is 1216.5 mAh/g, while the discharge specific capacity of the S@GA battery is 946.6 mAh/g, demonstrating that lithium−sulfur batteries based on S@GA/HNBRL electrodes have better charging and discharging performance. To compare the polarization levels of S@GA and S@GA/HNBRL during cycling, the voltage difference (ΔE) was calculated when both batteries reached a discharge−charge capacity of 600 mAh/g (Figure 7A). The ΔE value for the S@GA battery was 240 mV, significantly higher than that of the S@GA/HNBRL battery (129 mV). This is attributed to nitrogen doping introducing abundant defect sites and polar nitrogen functional groups, which strengthen the promote polysulfide binding and accelerate their redox kinetics. Figure 7B,C shows the magnified GCD curves of the different LSBs. The lowest overpotential observed for both Li_2S decomposition and precipitation in the S@GA/HNBRL demonstrates the significantly accelerated LiPS phase conversion kinetics. Figure 7D,E shows the charging and discharging testing curves of S@GA and S@GA/HNBRL at different rates. The graphs show that the charging and discharging capacitances of the batteries progressively decrease with the

https://doi.org/10.1021/acssuschemeng.5c06841
ACS Sustainable Chem. Eng. XXXX, XXX, XXX−XXX

increase of current. When the charging and discharging rates are lower, both electrode materials S@GA and S@GA/HNBRL exhibit more obvious charging and discharging platforms. In contrast, the charging and discharging plateau of the S@GA/HNBRL electrode is more pronounced at different rates, indicating that the electrode has higher electrochemical activity, thereby enabling the battery to achieve higher charging and discharging capacitance and a more stable cycling performance. According to previous reports, the conversion efficiency of sulfur during discharge has been defined as the capacity ratio between the second (Q2) and first (Q1) voltage plateaus.[60,61] Theoretically, the Q1 and Q2 correspond to 25% and 75% of the total capacity, respectively.[62] Thus, a Q2/Q1 ratio of 3 indicates complete conversion of S to Li_2S during discharge.[36,41,47,63] As shown in Figure 7F, S@GA/HNBRL exhibits the largest Q2/Q1 value, indicating that GA/HNBRL facilitates sulfur conversion and improves its utilization in LSBs.

Figure 7G shows the rate performance tests of S@GA and S@GA/HNBRL at different discharge rates. As shown, the discharge capacity of the S@GA/HNBRL electrode can reach 1216.5 mAh/g at a 0.2 C rate. With higher current densities, the discharge capacity of S@GA/HNBRL decreases. When the rate continues to increase to 2 C, its discharge capacity can be maintained at 480.5 mAh/g. As the rate is reduced back to 0.2 C, the capacity of the S@GA/HNBRL can still reach 938.2 mAh/g. In contrast, the S@GA electrode exhibited a discharge specific capacity of only 946.6 mAh/g at 0.2 C. With increasing current, the rate of battery fading intensified. At a rate of 2 C, the reversible capacity of the battery remained only at 471.1 mAh/g. By comparing the two kinds of electrodes, it can be found that S@GA/HNBRL exhibits a significantly better performance than the S@GA electrode at both high and low current. This result arises from the GA/HNBRL material not only retaining residual oxygen-containing groups but also introducing nitrogen atoms with multiple electrons, which expose more active sites. Through polar interactions, the adsorption capacity of the GA/HNBRL material for polysulfides is enhanced, which successfully prevents the shuttle effect of LSBs. Moreover, the introduction of HNBRL improves the physical and mechanical properties of the electrode material, which can significantly reduce the damage arising from sulfur volume changes to the electrode material.[64,65] Based on these advantages, the S@GA/HNBRL electrode exhibits a better rate performance and reversible performance than the S@GA electrode.

In order to further characterize the cycling stabilities of S@GA and S@GA/HNBRL electrode materials, we conducted 300 charge−discharge cycling stability tests. As shown in Figure 7H, the cell based on S@GA/HNBRL achieved the highest discharge specific capacity of 1347 mAh/g at 0.1 C. Moreover, its reversible capacity remained at 870.9 mAh/g after 300 cycles. The average capacity degradation rate per cycle is about 0.11%. In contrast, the initial discharge specific capacity of the S@GA electrode is only 1084.6 mAh/g at a 0.1 C rate. The reversible capacity of the cell decays to 482 mAh/g after 300 cycles, which is significantly lower than that of the S@GA/HNBRL electrode. The cycling performance of the batteries fabricated with S@GA and S@GA/HNBRL at a 1 C rate is shown in Figure 7I. The battery with S@GA/HNBRL can still provide a reversible specific capacity of 423.3 mAh/g even after 500 cycles, attributed to the strong LiPS adsorption and rapid redox reaction of Li_2S with GA/HNBRL. From the experimental results, it can be seen that lithium−sulfur batteries using S@GA/HNBRL electrodes exhibit a higher discharge capacity and superior cycling performance. To validate the performance of GA/HNBRL under lean-electrolyte conditions, long-cycle testing was conducted at an E/S ratio of 4.2 μL/mg at 1 C (Figure S13). The S@GA/HNBRL based LSB delivers an initial capacity of 565.8 mAh/g, and it is retained at 401.1 mAh/g after 400 cycles.

In addition, to eliminate the contribution from $LiNO_3$ decomposition during charge−discharge cycles, we assembled a battery using a blank GA/HNBRL (without S) as the cathode and conducted long-term cycling tests at 0.1 mA. As shown in Figures S14 and S15, the initial discharge specific capacity of the GA/HNBRL (without S) was 49.85 mAh/g. After 200 cycles, its discharge specific capacity degraded to 29.05 mAh/g. To further validate the mechanical and electrochemical stability of the GA/HNBRL electrode, we conducted cycling tests under sulfur loading conditions of 5.2 mg/cm^2. As shown in Figure S16, the initial discharge capacity of S@GA/HNBRL at 0.2 C was 955.1 mAh/g. After 200 cycles, its reversible capacity still reached 536.8 mAh/g, demonstrating excellent electrochemical stability. To further illustrate the enhancing effect of the S@GA/HNBRL electrode on reaction kinetics, for comparison, the S@GA/HNBRL electrode was evaluated against recently reported cathode materials, and the results are summarized in Table S3. Compared with other carbon based materials, batteries based on S@GA/HNBRL electrodes exhibit lower capacity decay and higher capacity. The experimental results indicate that lithium−sulfur batteries using S@GA/HNBRL electrodes have enhanced discharge capacity and improved cycling performance.

CONCLUSION

In summary, we successfully synthesized a nitrogen-doped porous aerogel material with high structural stability by a self-assembly method using hydrogenated nitrile butadiene rubber latex as a modifier. GA/HNBRL ensures efficient polysulfide adsorption and accelerated redox kinetics through the synergistic effects of physical adsorption and chemical anchoring, successfully mitigating the shuttle effect. The addition of HNBRL not only provides a kind of nitrogen source but also strengthens the mechanical performance of the carrier material. This achievement allows for higher S loading and limits volume change when used as a self-supporting material. Thanks to these advantages, the S@GA/HNBRL electrode can still achieve an initial discharge specific capacity of 1315.6 mAh/g at a 0.1 C rate without the involvement of current collectors, conductive agents, and binders. Furthermore, its discharge specific capacity can reach 870.9 mAh/g after 300 cycles at a 0.1 C rate. Importantly, the cell can still achieve a discharge specific capacity of 423.3 mAh/g after 500 cycles at a 1 C rate. This study presents innovative concepts for the application of self-supporting materials by integrating controllable porous structures with polymer materials.

ASSOCIATED CONTENT

Data Availability Statement

The data that have been used are confidential.

Supporting Information

The Supporting Information is available free of charge at https://pubs.acs.org/doi/10.1021/acssuschemeng.5c06841.

https://doi.org/10.1021/acssuschemeng.5c06841
ACS Sustainable Chem. Eng. XXXX, XXX, XXX−XXX

Additional experimental details, characterization methods for materials, testing conditions for batteries, optical images of samples, FTIR spectra, XPS spectra, TGA images, electrochemical performance data, electrical conductivity and EIS data comparisons, and electrochemical performance comparison with previously published self-supporting cathodes in LSBs (PDF)

Video S1: Compression experiment of GA/HNBRL (MP4)

AUTHOR INFORMATION

Corresponding Authors

Cunguo Wang − *State Key Laboratory of Advanced Optical Polymer and Manufacturing Technology, Key Laboratory of Rubber-plastics, Ministry of Education, Shandong Key Laboratory of High Performance Polyolefin Materials and Recycling, Qingdao University of Science and Technology, Qingdao, Shandong 266042, China;* orcid.org/0000-0001-8744-2220; Email: wangcg@qust.edu.cn

Aihua He − *State Key Laboratory of Advanced Optical Polymer and Manufacturing Technology, Key Laboratory of Rubber-plastics, Ministry of Education, Shandong Key Laboratory of High Performance Polyolefin Materials and Recycling, Qingdao University of Science and Technology, Qingdao, Shandong 266042, China*; Email: ahhe@qust.edu.cn

Seung Hee Lee − *Department of JBNU-KIST Industry-Academia Convergence Research, Jeonbuk National University, Jeonju 54896, Republic of Korea*; Email: lsh1@jbnu.ac.kr

Qi Li − *Suzhou Institute of Nano-Tech and Nano-Bionics (SINANO), Chinese Academy of Sciences (CAS), Suzhou, Jiangsu 215123, China;* orcid.org/0000-0002-0548-461X; Email: qli2013@sinano.ac.cn

Authors

Jixin Lu − *State Key Laboratory of Advanced Optical Polymer and Manufacturing Technology, Key Laboratory of Rubber-plastics, Ministry of Education, Shandong Key Laboratory of High Performance Polyolefin Materials and Recycling, Qingdao University of Science and Technology, Qingdao, Shandong 266042, China; Department of JBNU-KIST Industry-Academia Convergence Research, Jeonbuk National University, Jeonju 54896, Republic of Korea*

Mengyuan Zhu − *State Key Laboratory of Advanced Optical Polymer and Manufacturing Technology, Key Laboratory of Rubber-plastics, Ministry of Education, Shandong Key Laboratory of High Performance Polyolefin Materials and Recycling, Qingdao University of Science and Technology, Qingdao, Shandong 266042, China*

Lukuan Wang − *State Key Laboratory of Advanced Optical Polymer and Manufacturing Technology, Key Laboratory of Rubber-plastics, Ministry of Education, Shandong Key Laboratory of High Performance Polyolefin Materials and Recycling, Qingdao University of Science and Technology, Qingdao, Shandong 266042, China*

Chunjie Wu − *State Key Laboratory of Advanced Optical Polymer and Manufacturing Technology, Key Laboratory of Rubber-plastics, Ministry of Education, Shandong Key Laboratory of High Performance Polyolefin Materials and Recycling, Qingdao University of Science and Technology, Qingdao, Shandong 266042, China*

Yangyang Cui − *State Key Laboratory of Advanced Optical Polymer and Manufacturing Technology, Key Laboratory of Rubber-plastics, Ministry of Education, Shandong Key Laboratory of High Performance Polyolefin Materials and Recycling, Qingdao University of Science and Technology, Qingdao, Shandong 266042, China*

Qiaoling Bi − *State Key Laboratory of Advanced Optical Polymer and Manufacturing Technology, Key Laboratory of Rubber-plastics, Ministry of Education, Shandong Key Laboratory of High Performance Polyolefin Materials and Recycling, Qingdao University of Science and Technology, Qingdao, Shandong 266042, China*

Shaoyu Jiang − *State Key Laboratory of Advanced Optical Polymer and Manufacturing Technology, Key Laboratory of Rubber-plastics, Ministry of Education, Shandong Key Laboratory of High Performance Polyolefin Materials and Recycling, Qingdao University of Science and Technology, Qingdao, Shandong 266042, China*

Qing Zhao − *State Key Laboratory of Advanced Optical Polymer and Manufacturing Technology, Key Laboratory of Rubber-plastics, Ministry of Education, Shandong Key Laboratory of High Performance Polyolefin Materials and Recycling, Qingdao University of Science and Technology, Qingdao, Shandong 266042, China; Department of JBNU-KIST Industry-Academia Convergence Research, Jeonbuk National University, Jeonju 54896, Republic of Korea*

Xue Li − *State Key Laboratory of Advanced Optical Polymer and Manufacturing Technology, Key Laboratory of Rubber-plastics, Ministry of Education, Shandong Key Laboratory of High Performance Polyolefin Materials and Recycling, Qingdao University of Science and Technology, Qingdao, Shandong 266042, China*

Complete contact information is available at: https://pubs.acs.org/10.1021/acssuschemeng.5c06841

Notes

The authors declare no competing financial interest.

ACKNOWLEDGMENTS

The work described in this paper was supported by the National Natural Science Foundation of China (Grant No. 51972330), the Military Commission Logistics Department (Grant No. BY117J013), the State Key Program of National Natural Science Foundation of China (Grant No. 61734008), the National Key Research and Development Program of China (2022YFB3704700, 2022YFB3704702), the Major Scientific and Technological Innovation Project of Shandong Province (Grant No. 2021CXGC010901), and the Taishan Scholar Program of Shandong Province (Grant No. TS201511031). The authors also thank the support of Enchem Tianrun New Energy Materials (Shandong) Co., Ltd., Zaozhuang, Shandong, China (2023370203003384), and the Taishan Industrial Experts Program of Shandong Province (Grant No. tsls20241105).

REFERENCES

(1) Armand, M.; Tarascon, J.-M. Building better batteries. *nature* **2008**, *451* (7179), 652−657.

(2) Levi, M. D.; Wang, C.; Gnanaraj, J.; Aurbach, D. Electrochemical behavior of graphite anode at elevated temperatures in organic carbonate solutions. *J. Power Sources* **2003**, *119*, 538−542.

(3) Scrosati, B. Lithium rocking chair batteries: an old concept? *J. Electrochem. Soc.* **1992**, *139* (10), 2776.

(4) Pol, V. G.; Thackeray, M. M. Spherical carbon particles and carbon nanotubes prepared by autogenic reactions: Evaluation as anodes in lithium electrochemical cells. *Energy Environ. Sci.* **2011**, *4* (5), 1904−1912.
(5) Goodenough, J. B.; Park, K.-S. The Li-ion rechargeable battery: a perspective. *J. Am. Chem. Soc.* **2013**, *135* (4), 1167−1176.
(6) Zhang, W.; Sayavong, P.; Xiao, X.; Oyakhire, S. T.; Shuchi, S. B.; Vilá, R. A.; Boyle, D. T.; Kim, S. C.; Kim, M. S.; Holmes, S. E.; et al. Recovery of isolated lithium through discharged state calendar ageing. *Nature* **2024**, *626* (7998), 306−312.
(7) Zhao, L.; Sun, Y.; Zhao, Q.; Ullah, Z.; Zhu, S.; Zhu, M.; Liu, L.; Wang, C.; Li, Q.; He, A.; et al. Dual-type confinement strategy: Improving the stability of organic composite cathodes for Lithium-ion batteries with longer lifespan. *Chem. Eng. J.* **2024**, *490*, 151547.
(8) Pang, Q.; Liang, X.; Kwok, C. Y.; Nazar, L. F. Advances in lithium-sulfur batteries based on multifunctional cathodes and electrolytes. *Nature Energy* **2016**, *1* (9), 16132.
(9) Lin, Z.; Liu, Z.; Dudney, N. J.; Liang, C. Lithium superionic sulfide cathode for all-solid lithium-sulfur batteries. *ACS Nano* **2013**, *7* (3), 2829−2833.
(10) Jung, D. S.; Hwang, T. H.; Lee, J. H.; Koo, H. Y.; Shakoor, R. A.; Kahraman, R.; Jo, Y. N.; Park, M.-S.; Choi, J. W. Hierarchical porous carbon by ultrasonic spray pyrolysis yields stable cycling in lithium-sulfur battery. *Nano Lett.* **2014**, *14* (8), 4418−4425.
(11) Wang, Z.; Liu, L.; Zhu, M.; Sun, Y.; Zhao, Q.; Ding, Y.; Lu, J.; Wang, C.; Li, Q.; He, A.; Ye, F. Studies on the properties of 1, 5-diaminoanthraquinone (AAQ) composite used as new positive electrode material in lithium ion batteries. *Acta Chimica Sinica* **2024**, *82* (6), 589.
(12) Lu, J.; Zhu, M.; Kim, M.; He, A.; Wang, C.; Kim, T. H.; Lee, S. H. Catalytic nickel nanoparticles embedded on ZIF-8 backbone for accelerating polysulfide conversion in lithium-sulfur batteries. *J. Power Sources* **2025**, *647*, 237269.
(13) Das, S.; Bhuyan, M.; Gupta, K. N.; Okpowe, O.; Choi, A.; Sweeny, J.; Olawale, D.; Pol, V. G. Optimization of the form factors of advanced Li-S pouch cells. *Small* **2024**, *20* (31), 2311850.
(14) Li, H.; Wang, Z.; Dang, L.; Yu, K.; Yang, R.; Fu, A.; Liu, X.; Guo, Y.-G.; Li, H.; Zhao, X. S. Si nanoparticles enclosed in hierarchically structured dual-component porous carbon as superior anode for lithium-ion batteries: structure formation and properties investigation. *Energy Storage Mater.* **2024**, *70*, 103547.
(15) Wang, J.; Zhu, Y.-F.; Su, Y.; Guo, J.-X.; Chen, S.; Liu, H.-K.; Dou, S.-X.; Chou, S.-L.; Xiao, Y. Routes to high-performance layered oxide cathodes for sodium-ion batteries. *Chem. Soc. Rev.* **2024**, *53* (8), 4230−4301.
(16) Fan, W.; Chu, R.; Wang, C.; Song, H.; Ding, Y.; Li, X.; Jiang, M.; Li, Q.; Liu, L.; He, A. Synthesis and characteristic of the ternary composite electrode material PTCDA/CNT@ MPC and its electrochemical performance in sodium ion battery. *Composites Part B: Engineering* **2021**, *226*, 109329.
(17) Aurbach, D.; Lu, Z.; Schechter, A.; Gofer, Y.; Gizbar, H.; Turgeman, R.; Cohen, Y.; Moshkovich, M.; Levi, E. Prototype systems for rechargeable magnesium batteries. *Nature* **2000**, *407* (6805), 724−727.
(18) Yang, W.; Du, X.; Zhao, J.; Chen, Z.; Li, J.; Xie, J.; Zhang, Y.; Cui, Z.; Kong, Q.; Zhao, Z.; et al. Hydrated eutectic electrolytes with ligand-oriented solvation shells for long-cycling zinc-organic batteries. *Joule* **2020**, *4* (7), 1557−1574.
(19) Liu, X.; Huang, J.-Q.; Zhang, Q.; Mai, L. Nanostructured metal oxides and sulfides for lithium-sulfur batteries. *Adv. Mater.* **2017**, *29* (20), 1601759.
(20) Chu, R.; Nguyen, T. T.; Song, H.; Bai, Y.; Tran, D. T.; Kim, N. H.; Lee, J. H. Enriched vacancies of ruthenium doped niobium oxide on hollow graphene sphere as sulfur reduction reaction promoter in lithium sulfur batteries. *Applied Catalysis B: Environment and Energy* **2024**, *352*, 124030.
(21) Ye, Z.; Jiang, Y.; Li, L.; Wu, F.; Chen, R. A high-efficiency CoSe electrocatalyst with hierarchical porous polyhedron nanoarchitecture for accelerating polysulfides conversion in Li-S batteries. *Adv. Mater.* **2020**, *32* (32), 2002168.
(22) Xu, X.; Wang, S.; Wang, H.; Xu, B.; Hu, C.; Jin, Y.; Liu, J.; Yan, H. The suppression of lithium dendrite growth in lithium sulfur batteries: A review. *Journal of Energy Storage* **2017**, *13*, 387−400.
(23) Chu, R.; Nguyen, T. T.; Song, H.; P, M. A.; Bai, Y.; Kim, D. H.; Lee, J. H.; Kim, N. H. Crystal transformation engineering for effective polysulfides blocking layer for excellent energy density lithium-sulfur batteries. *Energy Storage Mater.* **2023**, *61*, 102877.
(24) Huang, T.; Sun, Y.; Wu, J.; Shi, Z.; Ding, Y.; Wang, M.; Su, C.; Li, Y. y.; Sun, J. Altering local chemistry of single-atom coordination boosts bidirectional polysulfide conversion of Li-S batteries. *Adv. Funct. Mater.* **2022**, *32* (39), 2203902.
(25) Gueon, D.; Hwang, J. T.; Yang, S. B.; Cho, E.; Sohn, K.; Yang, D.-K.; Moon, J. H. Spherical macroporous carbon nanotube particles with ultrahigh sulfur loading for lithium-sulfur battery cathodes. *ACS Nano* **2018**, *12* (1), 226−233.
(26) Chung, S.-H.; Manthiram, A. Current status and future prospects of metal-sulfur batteries. *Adv. Mater.* **2019**, *31* (27), 1901125.
(27) Xia, J.; Hua, W.; Wang, L.; Sun, Y.; Geng, C.; Zhang, C.; Wang, W.; Wan, Y.; Yang, Q. H. Boosting catalytic activity by seeding nanocatalysts onto interlayers to inhibit polysulfide shuttling in Li-S batteries. *Adv. Funct. Mater.* **2021**, *31* (26), 2101980.
(28) Piao, N.; Ji, X.; Xu, H.; Fan, X.; Chen, L.; Liu, S.; Garaga, M. N.; Greenbaum, S. G.; Wang, L.; Wang, C.; et al. Countersolvent electrolytes for lithium-metal batteries. *Adv. Energy Mater.* **2020**, *10* (10), 1903568.
(29) Chen, Y.; Wang, T.; Tian, H.; Su, D.; Zhang, Q.; Wang, G. Advances in lithium-sulfur batteries: from academic research to commercial viability. *Adv. Mater.* **2021**, *33* (29), 2003666.
(30) Wang, J.; Yi, S.; Liu, J.; Sun, S.; Liu, Y.; Yang, D.; Xi, K.; Gao, G.; Abdelkader, A.; Yan, W.; et al. Suppressing the shuttle effect and dendrite growth in lithium-sulfur batteries. *ACS Nano* **2020**, *14* (8), 9819−9831.
(31) Ma, L.; Lin, H.; Zhang, W.; Zhao, P.; Zhu, G.; Hu, Y.; Chen, R.; Tie, Z.; Liu, J.; Jin, Z. Nitrogen-doped carbon nanotube forests planted on cobalt nanoflowers as polysulfide mediator for ultralow self-discharge and high areal-capacity lithium-sulfur batteries. *Nano Lett.* **2018**, *18* (12), 7949−7954.
(32) Kim, J. H.; Seo, J.; Choi, J.; Shin, D.; Carter, M.; Jeon, Y.; Wang, C.; Hu, L.; Paik, U. Synergistic ultrathin functional polymer-coated carbon nanotube interlayer for high performance lithium-sulfur batteries. *ACS Appl. Mater. Interfaces* **2016**, *8* (31), 20092−20099.
(33) Xiao, Q.; Yang, J.; Wang, X.; Deng, Y.; Han, P.; Yuan, N.; Zhang, L.; Feng, M.; Wang, C. a.; Liu, R. Carbon-based flexible self-supporting cathode for lithium-sulfur batteries: progress and perspective. *Carbon Energy* **2021**, *3* (2), 271−302.
(34) Li, L.; Wu, Z.; Yuan, S.; Zhang, X.-B. Advances and challenges for flexible energy storage and conversion devices and systems. *Energy Environ. Sci.* **2014**, *7* (7), 2101−2122.
(35) Wang, H.-Y.; Dai, Y. K.; Liao, K.-M.; Deng, S.; Dai, G.-P. Vertical graphene growth on LDH nanosheets and carbon cloth nanofibers with NiCo nanoparticles as a freestanding host for high-performance lithium-sulfur batteries. *J. Phys. Chem. Lett.* **2025**, *16* (4), 1103−1113.
(36) Zhou, Q.-Y.; Tan, L.; Lv, T.-B.; Li, M.-C.; Zhang, J.-J.; Zhao, Z.-Q.; Jin, X.-J.; Liu, Z.; Hou, P.-P.; Zeng, Z.; et al. Nickel foam coated by Ni nanoparticle-decorated 3D nanocarbons as a freestanding host for high-performance lithium-sulfur batteries. *ACS Appl. Mater. Interfaces* **2023**, *15* (2), 3037−3046.
(37) Shi, H.; Zhao, X.; Wu, Z.-S.; Dong, Y.; Lu, P.; Chen, J.; Ren, W.; Cheng, H.-M.; Bao, X. Free-standing integrated cathode derived from 3D graphene/carbon nanotube aerogels serving as binder-free sulfur host and interlayer for ultrahigh volumetric-energy-density lithiumsulfur batteries. *Nano Energy* **2019**, *60*, 743−751.
(38) Su, D.; Cortie, M.; Wang, G. Fabrication of N-doped graphene-carbon nanotube hybrids from Prussian blue for lithium-sulfur batteries. *Adv. Energy Mater.* **2017**, *7* (8), 1602014.

https://doi.org/10.1021/acssuschemeng.5c06841
ACS Sustainable Chem. Eng. XXXX, XXX, XXX−XXX

(39) Liu, R.; Liu, W.; Bu, Y.; Yang, W.; Wang, C.; Priest, C.; Liu, Z.; Wang, Y.; Chen, J.; Wang, Y.; et al. Conductive porous laminated vanadium nitride as carbon-free hosts for high-loading sulfur cathodes in lithium-sulfur batteries. *ACS Nano* **2020**, *14* (12), 17308−17320.
(40) Yan, M.; Chen, H.; Yu, Y.; Zhao, H.; Li, C. F.; Hu, Z. Y.; Wu, P.; Chen, L.; Wang, H.; Peng, D.; et al. 3D ferroconcrete-like aminated carbon nanotubes network anchoring sulfur for advanced lithium-sulfur battery. *Adv. Energy Mater.* **2018**, *8* (25), 1801066.
(41) Li, M.-C.; Liu, Z.; Tan, L.; Zhou, Q.-Y.; Zhang, J.-J.; Hou, P.-P.; Jin, X.-J.; Lv, T.-B.; Zhao, Z.-Q.; Zeng, Z.; et al. Fabrication of cubic and porous carbon cages with in-situ-grown carbon nanotube networks and cobalt phosphide for high-capacity and stable lithium-sulfur batteries. *ACS Sustainable Chem. Eng.* **2022**, *10* (31), 10223−10233.
(42) Qin, B.; Zhao, X.; Wang, Q.; Yao, W.; Cai, Y.; Chen, Y.; Wang, P.; Zou, Y.; Cao, J.; Zheng, X.; et al. A tandem electrocatalyst with dense heterointerfaces enabling the stepwise conversion of polysulfide in lithium-sulfur batteries. *Energy Storage Mater.* **2023**, *55*, 445−454.
(43) Wang, C.; Song, H.; Yu, C.; Ullah, Z.; Guan, Z.; Chu, R.; Zhang, Y.; Zhao, L.; Li, Q.; Liu, L. Iron single-atom catalyst anchored on nitrogen-rich MOF-derived carbon nanocage to accelerate polysulfide redox conversion for lithium sulfur batteries. *J. Mater. Chem. A* **2020**, *8* (6), 3421−3430.
(44) Zhao, J.; Pan, R.; Sun, R.; Wen, C.; Zhang, S.-L.; Wu, B.; Nyholm, L.; Zhang, Z.-B. High-conductivity reduced-graphene-oxide/copper aerogel for energy storage. *Nano Energy* **2019**, *60*, 760−767.
(45) Song, P.; Zheng, S.; Ullah, Z.; Yang, Z.; Zhu, P.; He, A.; Wang, C.; Li, Q. Synergistic effects of FeCo bimetallic single-atom catalysts: accelerating the redox conversion of polysulfides and inhibiting the growth of lithium dendrites in lithium-sulfur batteries. *ACS Applied Energy Materials* **2023**, *6* (9), 4671−4682.
(46) Bai, Y.; Nguyen, T. T.; Chu, R.; Song, H.; Kim, N. H.; Lee, J. H. Heterostructured TiN/TiO_2 on the hierarchical N-doped carbon for enhancing the polysulfide immobilization and sulfur reduction in lithium-sulfur battery. *Chem. Eng. J.* **2023**, *476*, 146581.
(47) Song, H.; Nguyen, T. T.; Chu, R.; Bai, Y.; Kim, N. H.; Lee, J. H. Coupling interfacial effect in heterogeneous RuP_2-RuP for accelerating sulfur reduction reaction of lithium sulfur batteries. *Nano Energy* **2024**, *128*, 109859.
(48) Jeong, T.-G.; Choi, D. S.; Song, H.; Choi, J.; Park, S.-A.; Oh, S. H.; Kim, H.; Jung, Y.; Kim, Y.-T. Heterogeneous catalysis for lithium-sulfur batteries: enhanced rate performance by promoting polysulfide fragmentations. *ACS energy letters* **2017**, *2* (2), 327−333.
(49) Chu, R.; Nguyen, T. T.; Bai, Y.; Kim, N. H.; Lee, J. H. Uniformly controlled treble boundary using enriched adsorption sites and accelerated catalyst cathode for robust lithium-sulfur batteries. *Adv. Energy Mater.* **2022**, *12* (9), 2102805.
(50) Mahato, M.; Kim, J.-N.; Tabassian, R.; Rajabi-Abhari, A.; Kim, J.-S.; Nam, S.; Yoo, H.; Oh, I.-K. Mutually exclusive ytterbium and nitrogen co-doping of mesoporous titania-carbon for self-cleanable and sustainable triboelectric nanogenerators. *Nano Energy* **2021**, *90*, 106615.
(51) Mao, H.; Liu, L.; Shi, L.; Wu, H.; Lang, J.; Wang, K.; Zhu, T.; Gao, Y.; Sun, Z.; Zhao, J.; et al. High loading cotton cellulose-based aerogel self-standing electrode for Li-S batteries. *Science Bulletin* **2020**, *65* (10), 803−811.
(52) Ye, Z.; Jiang, Y.; Li, L.; Wu, F.; Chen, R. Self-assembly of 0D-2D heterostructure electrocatalyst from MOF and MXene for boosted lithium polysulfide conversion reaction. *Adv. Mater.* **2021**, *33* (33), 2101204.
(53) Wang, Y.; Deng, Z.; Huang, J.; Li, H.; Li, Z.; Peng, X.; Tian, Y.; Lu, J.; Tang, H.; Chen, L.; et al. 2D Zr-Fc metal-organic frameworks with highly efficient anchoring and catalytic conversion ability towards polysulfides for advanced Li-S battery. *Energy Storage Mater.* **2021**, *36*, 466−477.
(54) Gong, Q.; Hou, L.; Li, T.; Jiao, Y.; Wu, P. Regulating the molecular interactions in polymer binder for high-performance lithium-sulfur batteries. *ACS Nano* **2022**, *16* (5), 8449−8460.
(55) Liang, Z.; Yang, D.; Tang, P.; Zhang, C.; Jacas Biendicho, J.; Zhang, Y.; Llorca, J.; Wang, X.; Li, J.; Heggen, M. Atomically dispersed Fe in a C_2N based catalyst as a sulfur host for efficient lithium-sulfur batteries. *Adv. Energy Mater.* **2021**, *11* (5), 2003507.
(56) Lin, H.; Yang, L.; Jiang, X.; Li, G.; Zhang, T.; Yao, Q.; Zheng, G. W.; Lee, J. Y. Electrocatalysis of polysulfide conversion by sulfur-deficient MoS_2 nanoflakes for lithium-sulfur batteries. *Energy Environ. Sci.* **2017**, *10* (6), 1476−1486.
(57) Hu, S.; Yi, M.; Wu, H.; Wang, T.; Ma, X.; Liu, X.; Zhang, J. Ionic-liquid-assisted synthesis of N, F, and B Co-doped $CoFe_2O_{4-x}$ on multiwalled carbon nanotubes with enriched oxygen vacancies for Li-S batteries. *Adv. Funct. Mater.* **2022**, *32* (14), 2111084.
(58) Han, Z.; Zhao, S.; Xiao, J.; Zhong, X.; Sheng, J.; Lv, W.; Zhang, Q.; Zhou, G.; Cheng, H. M. Engineering d-p orbital hybridization in single-atom metal-embedded three-dimensional electrodes for Li-S batteries. *Adv. Mater.* **2021**, *33* (44), 2105947.
(59) Fan, F. Y.; Carter, W. C.; Chiang, Y.-M. Mechanism and kinetics of Li_2S precipitation in lithium-sulfur batteries. *Adv. Mater.* **2015**, *27* (35), 5203−5209.
(60) Xiao, W.; Kiran, G. K.; Yoo, K.; Kim, J.-H.; Xu, H. The dual-site adsorption and high redox activity enabled by hybrid organic-inorganic vanadyl ethylene glycolate for high-rate and long-durability lithium-sulfur batteries. *Small* **2023**, *19* (20), 2206750.
(61) Kim, Y.; Kim, W. I.; Park, H.; Kim, J. S.; Cho, H.; Yeon, J. S.; Kim, J.; Kim, Y.-J.; Lee, J.; Park, H. S. Multifunctional polymeric phthalocyanine-coated carbon nanotubes for efficient redox mediators of lithium-sulfur batteries. *Adv. Energy Mater.* **2023**, *13* (22), 2204353.
(62) Xu, J.; Yang, L.; Cao, S.; Wang, J.; Ma, Y.; Zhang, J.; Lu, X. Sandwiched cathodes assembled from CoS_2-modified carbon clothes for high-performance lithium-sulfur batteries. *Advanced Science* **2021**, *8* (16), 2101019.
(63) Ghosh, D.; Gad, M.; Lau, I.; Pope, M. A. Trapping and redistribution of hydrophobic sulfur sols in graphene-polyethyleneimine networks for stable Li-S cathodes. *Adv. Energy Mater.* **2018**, *8* (27), 1801979.
(64) Luo, X.; Pu, Z.; Li, H.; Zhao, E.; Yang, X.; Fu, A.; Liu, X.; Guo, Y.-G.; Li, H. Preparation of TiO_2 nanoparticles decorated porous carbon via a pseudo co-templating strategy and their application as substrates for high performance cathode of Li-S batteries. *J. Energy Storage.* **2024**, *102*, 114219.
(65) Luo, X.; Pu, Z.; Li, H.; Li, Z.; Yang, X.; Fu, A.; Liu, X.; Li, H. Co_2P nanoparticles decorated porous carbon nanofibers as self-standing cathode for high-performance Li-S batteries. *ACS Appl. Mater. Interfaces.* **2025**, *17* (26), 38019−38030.

https://doi.org/10.1021/acssuschemeng.5c06841
ACS Sustainable Chem. Eng. XXXX, XXX, XXX−XXX